How to cite: *Angew. Chem. Int. Ed.* **2022,** *61,* e202208534
International Edition: doi.org/10.1002/anie.202208534
German Edition: doi.org/10.1002/ange.202208534

CO_2 Reduction Reaction

Hydrophobicity Graded Gas Diffusion Layer for Stable Electrochemical Reduction of CO_2

Linbo Li, Jun Chen, Venkata Sai Sriram Mosali, Yan Liang, Alan M. Bond, Qinfen Gu,* and Jie Zhang**

Abstract: To mitigate flooding associated with the gas diffusion layer (GDL) during electroreduction of CO_2, we report a hydrophobicity-graded hydrophobic GDL (HGGDL). Coating uniformly dispersed polytetrafluoroethylene (PTFE) binders on the carbon fiber skeleton of a hydrophilic GDL uniformizes the hydrophobicity of the GDL and also alleviates the gas blockage of pore channels. Further adherence of the PTFE macroporous layer (PMPL) to one side of the hydrophobic carbon fiber skeleton was aided by sintering. The introduced PMPL shows an appropriate pore size and enhanced hydrophobicity. As a result, the HGGDL offers spatial control of the hydrophobicity and hence water and gas transport over the GDL. Using a nickel-single-atom catalyst, the resulting HGGDL electrode provided a CO faradaic efficiency of over 83 % at a constant current density of 75 mA cm^{-2} for 103 h operation in a membrane electrode assembly, which is more than 16 times that achieved with a commercial GDL.

[*] L. Li, V. S. S. Mosali, Y. Liang, A. M. Bond, J. Zhang
ARC Centre of Excellence for Electromaterials Science,
School of Chemistry, Monash University
Clayton 3800, Victoria (Australia)
E-mail: alan.bond@monash.edu
jie.zhang@monash.edu

J. Chen
ARC Centre of Excellence for Electromaterials Science, Intelligent Polymer Research Institute, Australian Institute for Innovative Materials, Innovation Campus, University of Wollongong
Squires Way, North Wollongong, NSW 2500 (Australia)

Q. Gu
Australian Synchrotron (ANSTO)
800 Blackburn Road, Clayton 3168, Victoria (Australia)
E-mail: qinfeng@ansto.gov.au

Introduction

Electrocatalytic reduction of CO_2 into valuable chemical feedstocks and fuels, driven by renewable energy, is an attractive route to realize a carbon-neutral economy.[1] To be commercially viable, the electrochemical CO_2 reduction reaction (ECO_2RR) with a stable current density (j) above 100 mA cm^{-2} at 80 % faradaic efficiency (FE) needs to be developed to offset the high capital costs.[2] Due to the low solubility and slow diffusion of CO_2 in aqueous electrolytes, a standard H-cell electrolyzer can only produce a j value of tens of mA cm^{-2}.[3] Overcoming this obstacle requires new electrolyzer systems and advanced catalysts.[4]

In a CO_2-gas-fed flow cell, the use of a gas diffusion electrode (GDE) with a catalyst layer deposited onto a porous hydrophobic gas diffusion lay (GDL), reduces the diffusion length of gaseous CO_2 to tens of nm, and provides access to j values greater than 1 A cm^{-2}.[5] A CO_2 gas-fed flow cell electrolyzer equipped with this type of GDE allows the ECO_2RR to occur at the gas-catalyst-electrolyte interface, which facilitates fast reaction kinetics.[5f,6] At this interface, the catalyst layer is required to balance the hydrophobicity needed for repelling water and the hydrophilicity for ionic conduction.[1d,5f] To ensure stability, a hydrophobic GDL, such as PTFE membrane GDL, can be used for repelling the aqueous electrolyte from the interface.[5f,6,7] Carbon GDLs, typically made of porous carbon fiber supports (CFS) and a microporous layer, have been widely used in fuel cells.[7a,8] However, rapid hydrophobicity degradation due to electrolyte salt precipitation or increase in hydrophilicity of the exposed carbon fiber surface under electrolysis conditions, leads to limited longevity.[4a,9] These types of GDEs commonly suffer from electrolyte flooding within several hours under ECO_2RR conditions, in part because carbon GDLs are not tailor-made for use with the ECO_2RR.[3c,9,10]

To stabilize a GDL for the ECO_2RR application, a comprehensive understanding of the mechanisms within the GDL and the catalyst layer is needed. Porosity and hydrophobicity, which have a significant effect on capillary pressure, are the critical parameters to control gas and water transport.[6,11] According to the Young–Laplace equation,[11] a GDL with a large pore/crack size or a low contact angle will have a low capillary pressure to resist liquid intrusion and hence suffers a higher risk of flooding. Functionalization of a catalyst with a fluorine-terminated silane or dispersion of PTFE nanoparticles inside the catalyst layer could increase GDE stability against flooding from a few hours to

slightly more than ten hours.[6,9a,12] This limited improvement by these strategies is attributed to the fact that the carbon GDL is only partially covered with PTFE since the uncovered region is needed for current collection.[3c,13] Alternatively, a PTFE GDE, where the hydrophobic PTFE-membrane GDL and current collector are decoupled, can stabilize the flow cell operation for over one hundred hours.[3c,5f,7a,14] However, the inherently insulating PTFE membrane significantly increases the internal electrical resistance of the cell. To enhance electron transport under these circumstances requires sputtering with a thick layer of a metallic catalyst, such as Ag, Cu and Au.[1d,7b,c,15] This restricts applications of catalysts that cannot be sputtered or have low electrical conductivity.

By combining the structural features of both carbon and PTFE membrane GDLs, we here introduce a hydrophobicity-graded process that converts a hydrophilic carbon GDL into a hydrophobicity-graded carbon GDL (HGGDL). The HGGDL has a narrow pore size distribution, spatially differentiated hydrophobicity as well as porosity and permeability. It also consists of a hydrophobicity-homogenized carbon fiber skeleton (CFS, containing 5–10 wt % of PTFE binder) coupled with a hydrophobic PTFE macroporous layer with a loading of 10–20 wt %. The hydrophobicity-graded method includes CFS hydrophobization and local hydrophobicity enhancement processes. The former process aims to achieve uniform hydrophobicity of the CFS while maintaining an optimal porosity in order to facilitate the transport of gas (avoid gas blocking) during electrolysis. The latter process decouples the functions of water repelling and current collection with the GDL via binding a PTFE macroporous layer to one side of the GDL. Atomically dispersed nitrogen coordinated nickel (NiN_4) sites on a carbon black support (NiNCB), which reduces CO_2 to CO, is selected as a model catalyst to assess the stability of the HGGDL. The GDE is stable for at least 103 h, which is 16 times more that achieved by a commercial hydrophobic carbon GDL. The GDL fabrication strategy could be used to fabricate GDLs for other electrolysis and energy conversion applications.

Results and Discussion

Atomic Ni sites coordinated with nitrogen atoms in a carbon black matrix (NiNCB) were synthesized by a cheap, simple and scalable pyrolysis method (Scheme S1).[16] The NiNCB was used here not only as an ECO_2RR catalyst but also as a microporous layer. Structural information of NiNCB was characterized using electron microscopy and spectroscopy. No nanoparticles or atomic clusters derived from crystalline Ni species were observed by scanning electron microscopy (SEM) or transmission electron microscopy (TEM) (Figure S1 and Figure S2). No carbide, nitride, oxide or metallic Ni species were detected by powder X-ray diffraction (XRD) or Raman spectroscopy (Figure S3).[17] The X-ray photoelectron spectrometry (XPS) spectra including C 1s and O 1s of NiNCB, showed similar peak features to those of N-doped carbon black (NCB), while the peak at 398.7 eV in the N 1s XPS spectrum of NiNCB shifted positively by ≈0.3 eV versus that of NCB (Figure S4). These results implied that Ni atoms in NiNCB coordinate with N much more strongly than C or O. Further XPS fitting analyses have revealed the presence of the pyridinic (398.4 eV), pyrrolic (400.7 eV), graphitic (402.7 eV), and oxidized (405.3 eV) N species in NCB (Figure S5, top). Positively shifted pyridinic N (398.6 eV) in NiNCB is assigned to its protonated counterpart due to the decrease of electron density surrounding the N atom, resulting from the coordination effect between Ni and N (Figure S5, bottom).[18] A new peak at 399.6 eV in NiNCB corresponds to Ni-coordinated N species (Figure S5).[17b] Note that the C content of NiNCB was increased at the expense of O and N relative to those found in the NCB, indicating a promoted carbonization and conductivity to NiNCB (Figure S4b–d and Table S1). This partially accounts for the enhanced electrochemical surface area and current density for NiNC compared with NCB (Figure S6).

High-angle annular dark-field scanning transmission electron microscopy (HAADF-STEM) images and corresponding energy dispersive x-ray spectroscopy (EDS) mapping images demonstrated the uniform dispersion of C, N, O, and Ni atoms throughout the NiNCB substrate (Figure 1a). The single bright dots with a size of ≈0.2 nm confirmed the atomic dispersion of Ni sites in the NiNCB matrix (Figure 1b). Analysis of the Ni K-edge X-ray absorption near-edge structure (XANES) spectra (Figure 1c) and Ni 2p XPS spectra (Figure S4e) revealed that the average oxidation state of Ni species in NiNCB was +1.2 (Table S2).[19] The Ni K-edge extended X-ray absorption fine structure (EXAFS) spectrum confirmed the atomic nature of Ni–N sites in NiNCB (Figure 1d and Figure S7). The fitted EXAFS results suggested that the average coordination number of Ni in the catalyst was 4 and that Ni center renders a planar NiN_4 structure in NiNCB (Figure 1d,e and Table S2).

The ECO_2RR performances with NiNCB were initially tested in a flow cell using 1 M KOH as the electrolyte with a commercial hydrophobic carbon GDL, i.e., Toray TGP-H-60 (TGP60, PTFE loading: ≈5 wt %) (Figure S8). Use of either CB or NCB produced mainly H_2 with a tiny amount of formate over the potential range of −0.2 V to −1.0 V versus the reversible hydrogen electrode (RHE) (All potentials reported in this paper are with respect to the RHE reference unless otherwise stated) (Figure S9). In contrast, NiNCB produced CO as the major CO_2 reduction product over the potential range of −0.15 V to −0.80 V (Figure 1f,g and Figure S10). In this potential range, the maximum FE_{CO} of 95.4 % was obtained at ≈−0.45 V and the maximum j_{CO} of ≈127 mA cm^{-2} was obtained at ≈−0.59 V. The stability of NiNCB/TGP60 GDE was further studied in 1 M KOH at −0.59 V, at which the FE_{CO} is ≈91 % (Figure 1h). With this GDL, operational stability suffered from dramatic current oscillation due to gas blocking in the gas channels of the GDL (Figure 1h). The electrolysis was terminated after 5 min because electrolyte flooding was observed. The poor stability found in the

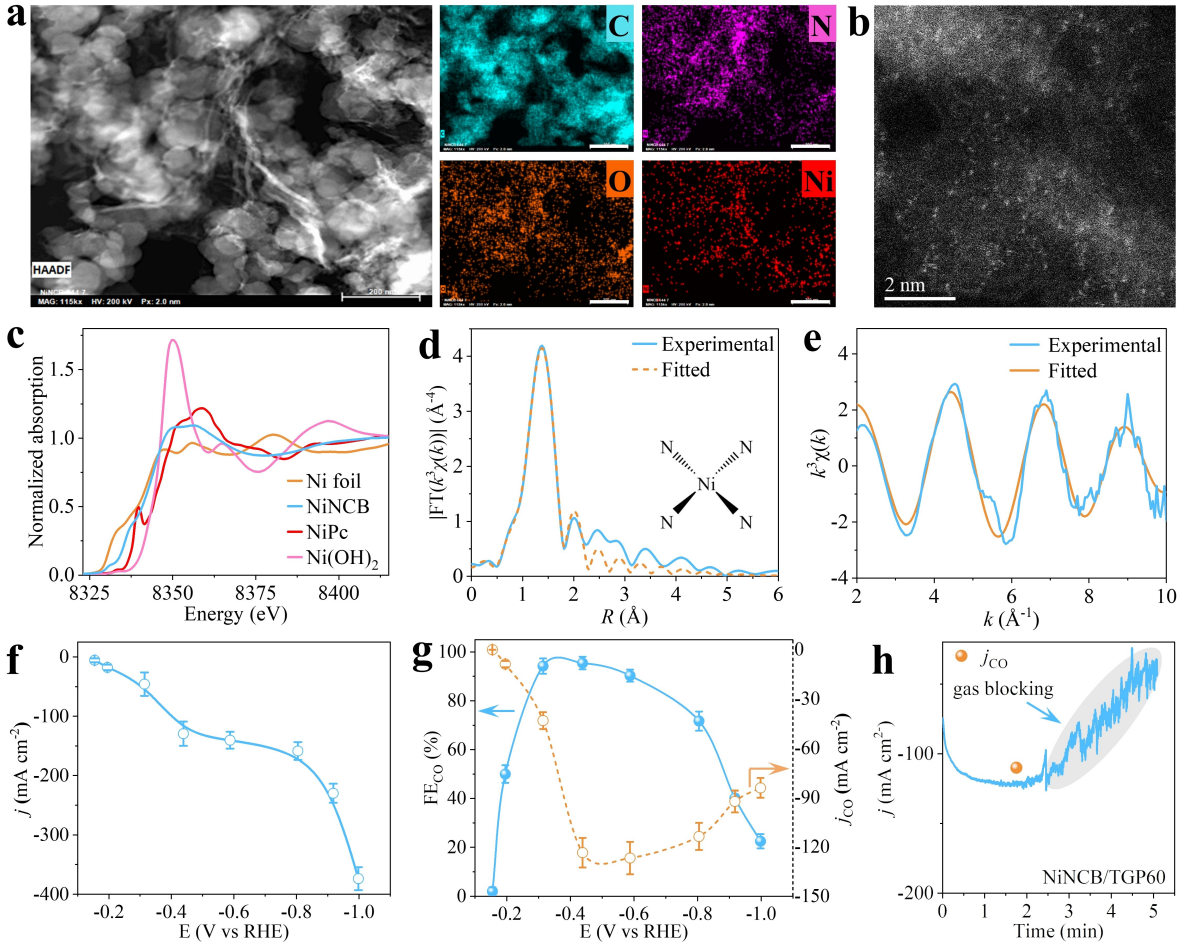

Figure 1. Characterizations of NiNCB. a) HAADF-STEM image and the corresponding EDS mapping for C, N, O, and Ni elements. Scale bars: 200 nm. b) Aberration-corrected HAADF-STEM image. Scale bar: 2 nm. c) Fourier-transformed (FT) Ni K-edge XANES spectra (cyan) with reference samples (Ni foil-yellow, nickel phthalocyanine (NiPc)-red and $Ni(OH)_2$-pink). d,e) Ni K-edge EXAFS analysis in *R* and *k* spaces. f) Total *j*. g) FE and partial *j* of CO. h) Stability of NiNCB/TGP60 GDE at −0.59 V. The stability test was terminated after 5 min when flooding was observed. The shaded area highlights the dramatic current oscillation caused by gas blocking.

NiNCB/TGP60 GDE indicates the used commercial GDL configuration is not suitable for ECO_2RR.

To reveal the origin of the poor stability of the NiNCB/TGP60 GDE during ECO_2RR, the morphology, hydrophobicity, porosity and pore size distribution of TGP60 were investigated by microscopic and spectroscopic techniques. SEM images coupled with EDS mapping analyses suggested that a wide range of CFS in the GDL were covered by highly coalescent, bulky and nonconductive PTFE film, which provided low porosity and hinders efficient mass transfer at the catalyst/GDL interface (Figure 2a and Figure S11). This could be responsible for the current oscillation in connection with gas blocking (Figure 1h). The ECO_2RR stability of the catalyst-free TGP60 electrode was also examined under the same operating conditions as used with a NiNCB/TGP60 GDE. Chronoamperometric measurement showed that the bare TGP60 electrode could sustain a stable current density for a longer period. Furthermore, current oscillation due to gas blocking was not observed in the absence of the catalyst/GDL interface, although flooding still occurred after ≈35 min (Figure 2b). XPS and contact angle measurements were applied to probe hydrophobicity changes on the bare TGP60 during the flooding process (Figure 2c,d). O 1s high-resolution XPS spectra and deconvoluted data revealed that the overall oxygen content and oxygen-containing hydrophilic functional groups (especially for the carboxylic group) on the surface increased with electrolysis time (Figure 2c).[20] This indicated that hydrophilicity and carbonate/bicarbonate concentration on the bare TGP60 surface had increased during electrolysis. The hydrophobicity loss of TGP60 was further confirmed by a downward trend for the contact angle with electrolysis time (Figure 2d).

The above findings indicate that the commercially available wet-proof carbon GDL needs to be reconstructed to accommodate ECO_2RR applications, especially for stability. Accordingly, a hydrophobicity-engineering method is introduced to transform a hydrophilic carbon GDL into a hydrophobicity-graded carbon GDL (HGGDL) having a narrow pore size distribution as well as spatially differentiated hydrophobicity. The hydrophobicity-graded approach includes two successive and separate processes: CFS-

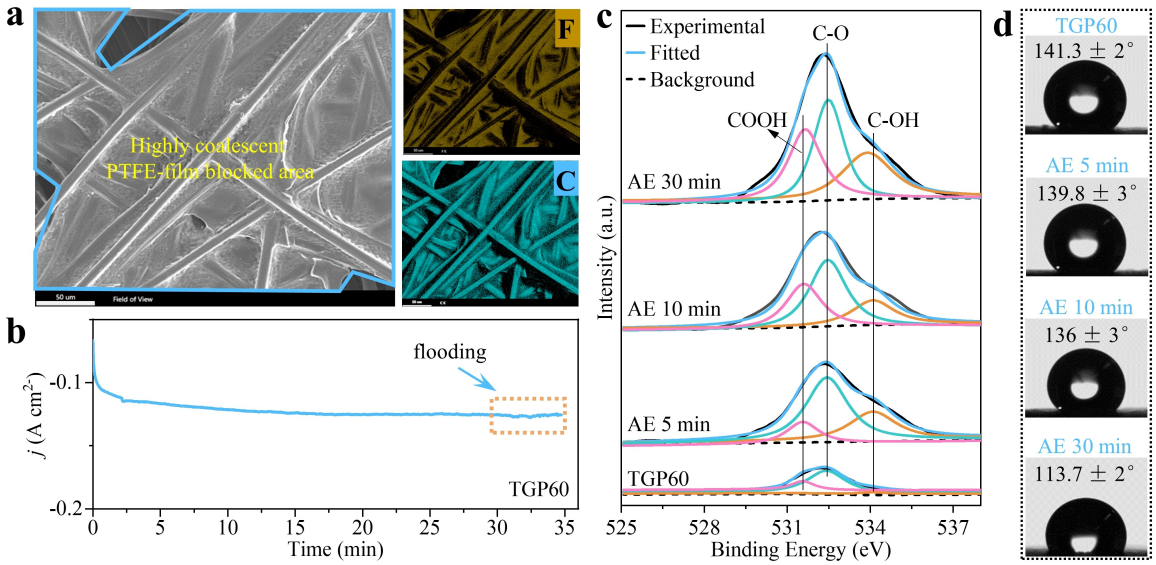

Figure 2. a) SEM image and EDS mapping images of F (yellow) and C (cyan), scale bar: 50 μm. b) Chronoamperometric measurements with a bare TGP60 in 1 M KOH at −0.59 V. Measurement was terminated when flooding was observed. c,d) Deconvoluted high-resolution O 1s XPS spectra and contact angles for TGP60 as a function of electrolysis time. AE: time after electrolysis commenced.

skeleton hydrophobization and local hydrophobicity enhancement (see Methods for details). The CFS-skeleton hydrophobization process is mainly aimed at achieving a uniform distribution of the hydrophobic binders on the whole skeleton of the hydrophilic GDL while sustaining high porosity. The hydrophobization method utilizes a series of steps in the order of PTFE dipping, hexane cleaning, airbrush blowing and sintering (Figure 3a). To illustrate the process, the raw hydrophilic TGP GDL (HTGP) used for preparing the commercial TGP60 is considered (Figure S8 and Figure S12). In this example, a piece of HTGP was firstly dipped in a PTFE emulsion. The PTFE-treated HTGP was then cleaned with hexane (Figure 3b).

The effect of the cleaning step on the porosity of HTGP was examined using acetone, methanol, ethanol, 2-propanol, 1-butanol and hexane solvents having different polarities (Figure 3c and Figure S13). A negative correlation between the solubility of organic solvent in water and the porosity of HTGP was found (Figure 3c). The PTFE emulsion is an oil-in-water (O/W) system. Accordingly, when the solubility of organic solvent (or its polarity) in water decreases, the demulsification effect declines and even disappears in the case of hexane cleaning (Figure S13). This result is consistent with SEM images which show that the coverage of PTFE blocks on CFS and blockage of the gas pores of the GDL, decrease with a reduction in polarity of organic solvents, in agreement with the relationship between the solubility of organic solvent in water and porosity of the treated HTGP (Figure 3c and Figure S14). After hexane cleaning, the hydrophobicity and surface C–F_2 content of PTFE-treated HTGP are enhanced at the expense of that of C–C and C–O species (Figure S15a–d). This finding indicates that the hexane washing efficiently removes the nonionic surfactant component of the PTFE emulsion, giving a highly hydrophobic surface. During cleaning, the internal PTFE emulsion in the HTGP was replaced by hexane (Figure S15e,f). This effect is attributed to the water insolubility of hexane, which leads to improved porosity of the resultant GDL (Figure 3c). Note that the stratified PTFE emulsion in hexane can be extracted for reuse (Figure S15g). After washing, the treated HTGP skeleton was blown with high-speed N_2 using an airbrush, in order to remove PTFE residues while drying the skeleton (Figure S16). The resultant GDL is denoted as PTGP (PTFE-dipped HTGP, 5–10 wt % of PTFE loading). Inspection of the SEM images revealed that the airbrush blowing step minimized residual PTFE emulsion blockage to the HTGP pore channels no matter whether it was cleaned by polar or nonpolar solvents (Figure S17).

The final sintering step was performed at 320 °C, which is close to the melting point of PTFE (327 °C). This step strengthens the adhesion of the hydrophobic PTFE binders to the CFS, leading to an improved hydrophobicity over the PTGP (Figure S18a). Mercury intrusion porosimetry (MIP) analysis confirmed that the pore size distribution of PTGP is similar to that of the pristine HTGP while the average pore size of PTGP is larger than that of commercial TGP60 (Figure S18b and Table S3). Visual inspection of TGP60 and PTGP with an optical microscope supported this conclusion (Figure 3d–g). Examination of cross-sectional/top-view SEM images and EDS mapping results reveals that the hydrophobic PTFE nanorods are uniformly distributed over the entire PTGP skeleton with no PTFE blocks or films found (Figure 2a, Figure 3h and Figure S19). In contrast, PTFE coating was mostly present on two surface layers of TGP60 (Figure 2a, Figures 3i,j and Figure S11). Accordingly, the electrochemical surface area of the porous PTGP was estimated to be ≈4 times that of TGP60 (Figure S20). Thus, the PTGP with CFS skeleton hydrophobization exhibits higher porosity and more uniform hydrophobicity with a

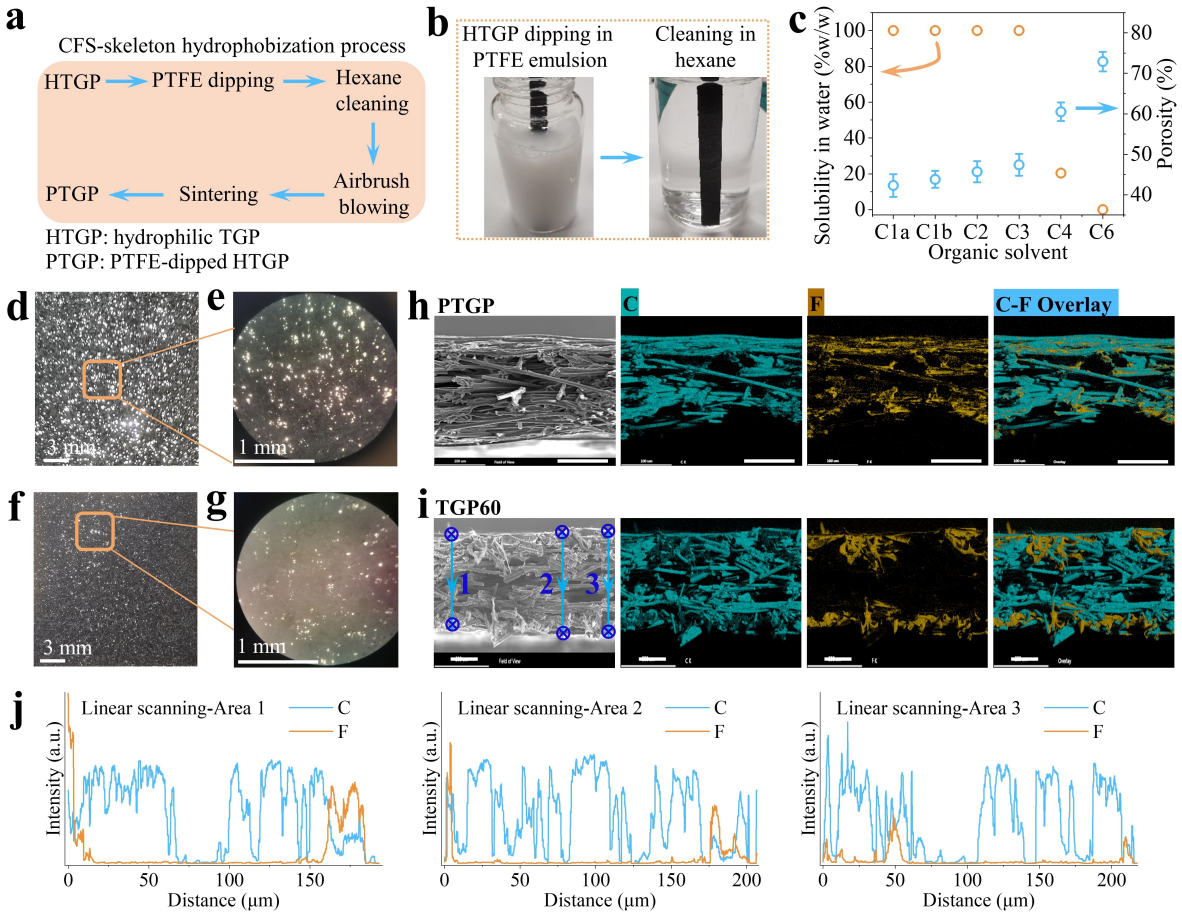

Figure 3. a) Schematic representation. b) Demonstration of PTFE dipping and hexane cleaning steps. c) Correlation between type of organic solvent (C1a: acetone; C1b: methanol; C2: ethanol; C3: 2-propanol; C4: 1-butanol; C6: hexane) and the solubility in water and the porosity of the PTGP (sintered). Error bars represent one standard deviation based on three independent experiments. d–g) Visual inspection of pore features for GDLs using an optical microscope: PTGP (d) and TGP60 (f). e,g) Zoom-in images of the designated areas in(d) and (f), respectively. h,i) Cross-sectional SEM and EDS mapping images: PTGP (h) and TGP60 (i). Scale bar: 100 μm. j) SEM-EDS linear scanning (top-down) profiles are measured from 3 areas labelled 1, 2 and 3 in (i). The distances reported are relative to the top surface.

larger active surface area in comparison with commercial TGP60. This lays the foundation for a strategy to regulate the hydrophobicity as well as the activity of catalyst layer adjacent to the CFS and reduce the risk of the gas blocking of the PTGP.

One side of the PTGP was further modified with a hydrophobic PTFE macroporous layer (PMPL) via the local hydrophobicity enhancement process in order to decouple the current collection and hydrophobicity requirements. To achieve this, one side of PTGP was coated with a layer of PTFE emulsion by brushing or spraying the CFS surface with PTFE emulsion (Figure 4a–c and Figure S21). The coated PTGP was then subjected to a series of airbrush blowing, hexane cleaning and sintering treatments similar to those described above for the CFS-skeleton hydrophobization process (Figure 3a). The final GDL product without sintering is denoted as unsintered HGTGP. The PTFE nanorods of PMPL on unsintered HGTGP were compactly stacked (Figure 4d). A volcano-shaped relationship is observed between the sintering temperature and MIP-porosity as well as contact angle (Figure 4f, Figure S22 and Table S3). A sintering step was then introduced at 320 °C to enhance the adhesion of PMPL. Due to the decrease of overall interfacial free energy driving by sintering,[21] the sintered PTFE nanorods of PMPL on HGTGP shrink and coalesce to give a bridged and macroporous hydrophobic network with enhanced hydrophobicity (Figure 4e and Figure S23a,b). Coating PMPL on PTGP barely changes the electrical conductivity of PTGP (Figure S23c). The cross-sectional SEM and EDS results confirmed the presence of a graded distribution of PTFE nanorods from the carbon fiber skeleton to the PMPL, i.e., graded hydrophobicity over HGTGP (Figures 4g–j). Data in Table S3 show that both porosity and permeability of the as-prepared PTGP are larger than with TGP60 and significantly larger than with PMPL (Figure S23d–f). In this study, HGTGP is regarded as the PMPL coated PTGP. The PTFE macroporous layer with lower porosity and gas permeability mitigates excess CO_2 input across the electrode. PTGP with larger porosity and gas permeability ensures that CO_2 has access to the catalyst layer. These results emphasize that the HGTGP has graded hydrophobicity, narrow pore size distribution, porosity and

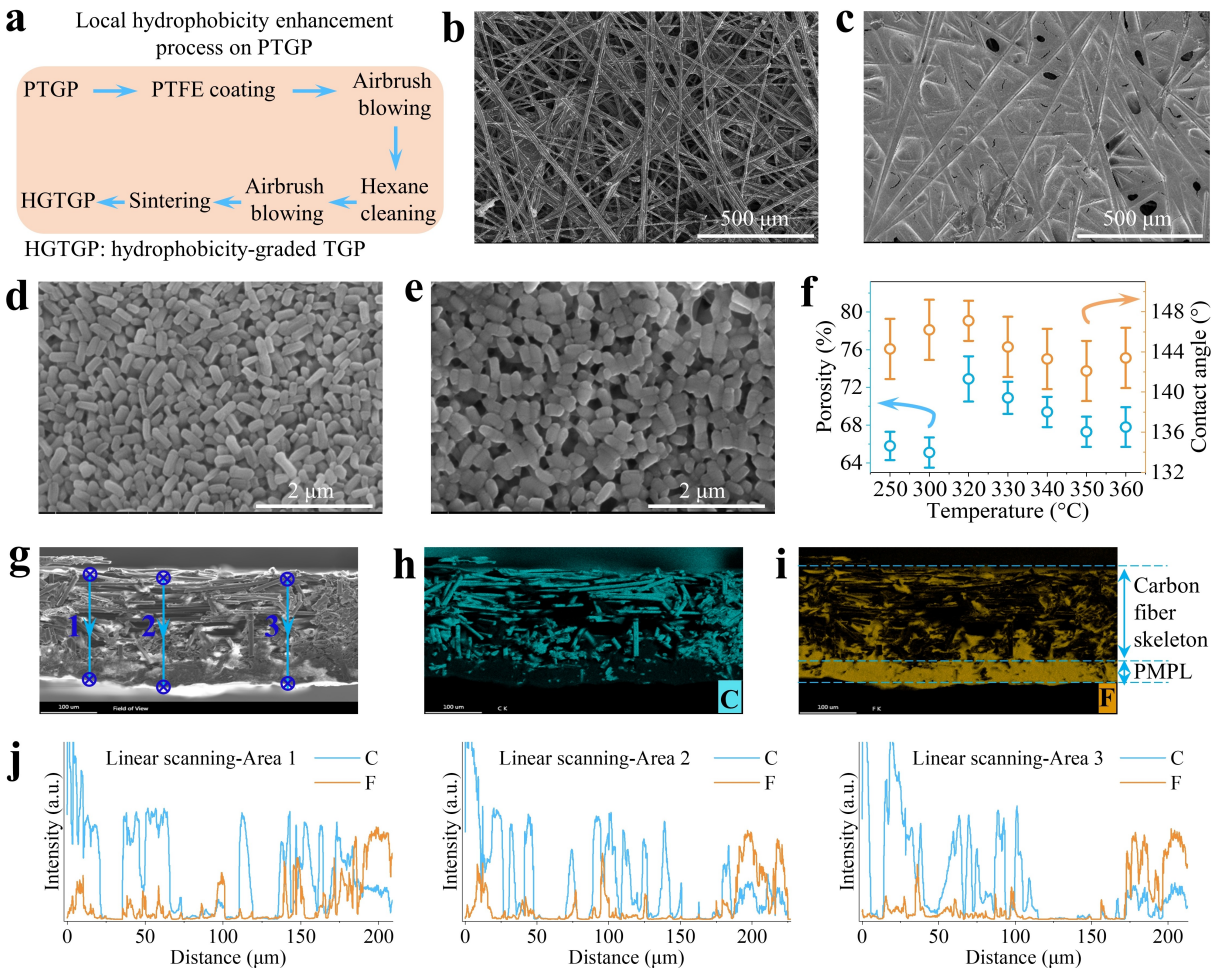

Figure 4. a) Schematic representation of the GDL fabrication process. b,c) Low-magnification SEM images of PTGP and unsintered HGTGP, respectively. d,e) High-magnification SEM images of unsintered HGTGP and sintered HGTGP (320 °C), respectively. f) Correlation between sintering temperature and the contact angle (Figure S22a–g) as well as MIP-porosity (Figure S22h) of HGTGP. Cross-sectional image (g) and corresponding EDS mapping for C (h) and F (i) of HGTGP sintered at 320 °C. PMPL: PTFE macroporous layer. j) SEM-EDS linear scanning (top-down) profiles are measured from 3 areas labelled 1, 2 and 3 in g). The distances reported are relative to the top surface.

permeability, which is responsible for the remarkably enhanced stability of the CO_2 reduction (vide infra).

The effect of sintering temperature on the ECO_2RR performance of the HGTGP-based electrode was evaluated using a liquid flow-cell setup under conditions similar to those used for NiNCB/TGP60 GDE stability testing. Compared with the NiNCB/TGP60 GDE, the operational current of the NiNCB/unsintered HGTGP GDE was more stable and the duration for stability extended to 30 min (Figure 1h and Figure S23g). This limited improvement in durability of unsintered HGTGP-based GDE suggests that the GDL still cannot repel water intrusion efficiently without a robust and coalescent hydrophobic network of PMPL attached to the CFS (Figure 4d and Figure S23a,b). The durability of all the GDEs using HGTGP sintered over the temperature range of 250 to 360 °C was improved with only HGTGP sintered at 250 °C encountering flooding after ≈1.3 h (Figure S24). Presumably, the low coalescent level of PTFE nanorods at 250 °C leads to inadequate hydrophobicity and capillary pressure to withstand electrolyte percolation. With the HGTGP sintered at 300 °C, the current oscillation was observed when the CO_2 gas supply was interrupted, which rapidly disappeared after resuming the CO_2 gas supply. These features are associated with obstruction by back pressure attributed to inadequate porosity and pore size, which requires additional or external pressure to drain water and gas from the interior of the GDL.[22] GDEs based on HGTGP sintered at above 350 °C also encountered gas blocking issues, resulting from the overly coalescent PTFE nanorods. Thus, the sintering temperature range for HGTGP of 320 °C to 340 °C was optimal and 320 °C was selected as the sintering temperature for further applications.

The examination of the influence of PTFE loading on the stability of NiNCB/HGTGP GDEs revealed that the optimal PTFE loading on HGTGP was in the range of 20 wt % to 30 wt % (Figure S25). Evaluation of SEM images and contact angles of PMPL coupled with HGTGP before and after 12 h of electrolysis confirmed the pore size distribution and hydrophobicity remained stable and hence

that the resistance to electrolyte percolation has been achieved (Figure S26).

To verify the viability of the hydrophobicity graded strategy, the NiNCB/TGP60 (Figure 5a) or NiNCB/HGTGP (Figure 5b) GDE cathode was integrated into a home-made membrane electrode assembly (MEA) cell. The MEA cell was run at a constant current density of 75 mA cm^{-2} using an IrO_x/Ti mesh anode in a 0.1 M $KHCO_3$ anolyte (Figure S27).[23] Under these conditions, the NiNCB/TGP60 cathode provided a stable FE_{CO} of 90 % for ≈5 h with an average full-cell voltage of 3.65 V. However, gas blocking and flooding occurred in ca. 6 h, which caused the FE_{CO} of NiNCB/TGP60 cathode to rapidly fell below 25 % (Figure 5c). Under similar conditions, the life of the NiNCB/HGTGP cathode with a stable FE_{CO} of 90 % was extended to 77 h and had a slightly improved average full-cell voltage of 3.57 V. The lower MEA cell potential is attributed to the higher active surface area of PTGP than that of TGP60 and hence boosted reaction kinetics on the surface of PTGP (Figure S20). ECO_2RR operation for NiNCB/HGTGP cathode with FE_{CO} above 83 % was sustained for 103 h, which is more than 16 times that of the commercial TGP60 based counterpart (Figure 5d). The MEA cell slowly ran into flooding after ≈116 h as evidenced by the commencement of current oscillations and a significant loss of FE_{CO}. Cathode variations for both the NiNCB/TGP60 and NiNCB/HGTGP electrodes after electrolysis also were investigated. Examination of Figure S28 reveals that the enhanced ECO_2RR stability of NiNCB/HGTGP cathode benefits from the mitigated K^+ permeation in the hydrophobicity-graded electrode.

Conclusion

A hydrophobicity-engineering method has been used to transform a hydrophilic carbon GDL into a hydrophobicity-graded one using a series of steps, including PTFE dipping/coating, hexane cleaning, airbrush blowing and sintering. The newly developed hydrophobicity-graded GDL contains a hydrophobic CFS-skeleton with high porosity and spatially uniform hydrophobicity, which is also coated with a compact hydrophobic PTFE macroporous layer to provide a modest pore size and achieve enhanced hydrophobicity. Under liquid flow-cell conditions, a NiNCB/HGGDL cathode exhibited improved water and gas transport, and offered substantial resistance to electrolyte flooding. Using a MEA cell equipped with this cathode, CO_2 to CO conversion with a FE_{CO} is obtained for above 83 % over 103 h of operation with a constant current density of 75 mA cm^{2-} in a neutral medium. The lifetime of the hydrophobicity-graded electrode is more than 16 times longer than that of a commercially available GDL-based counterpart. This study demonstrates the advantages of using a GDL with a graded hydrophobicity structure and modest pore size distribution for long-term CO_2 electrolysis. To further stabilize the ECO_2RR, future work is required to optimize the hydrophobicity distribution, pore size and gas permeability of HGGDL to prevent electrolyte flooding. In parallel, superior anion exchange membranes are needed to minimize K^+ crossover.

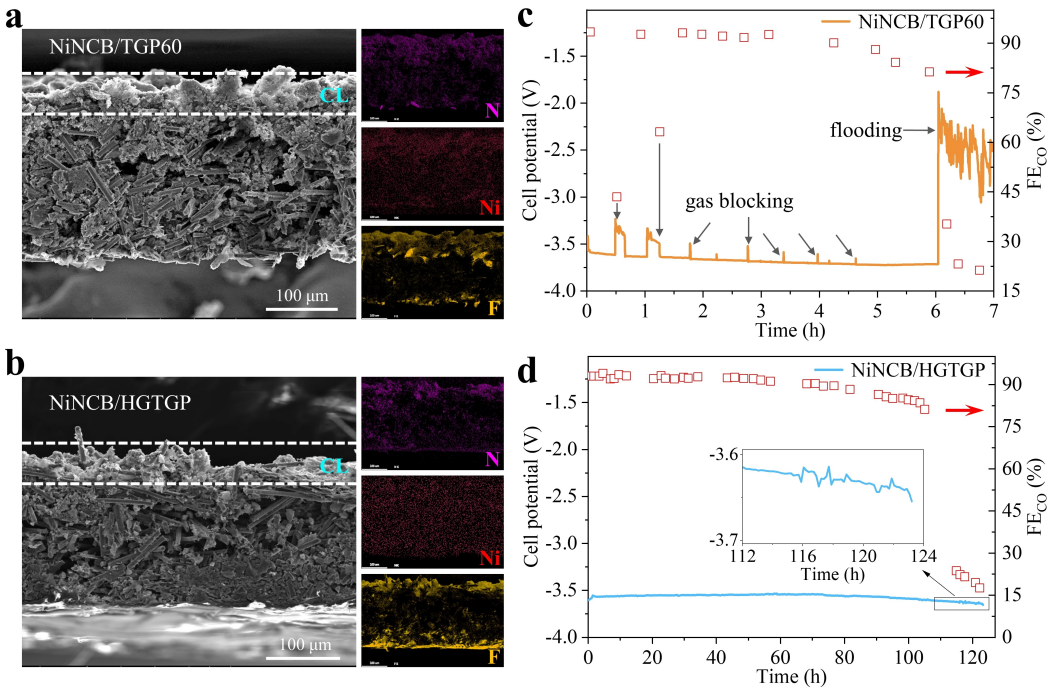

Figure 5. The cross-sectional SEM and EDS mapping (N, Ni, F) images of cathode GDEs: NiNCB/TGP60 (a) and NiNCB/HGTGP (b), CL: catalyst layer. MEA-stability measurements using a 0.1 M $KHCO_3$ anolyte under a constant current density of 75 mA cm^{-2} with a cathode: NiNCB/TGP60 (c) and NiNCB/HGTGP (d).

Acknowledgements

This research was supported by the Australian Research Council (ARC) through the ARC Centre of Excellence for Electromaterials Science (grant no. CE140100012) and the Discovery Project Scheme (grant no. DP220100316 and grant no. DP 220101290). This research was undertaken on the XAS beamline at the Australian Synchrotron, part of ANSTO. The authors acknowledge Zhou Xu for sample coating and the Monash Centre for Electron Microscopy for use of equipment funded by the Australian Research Council (grant no. LE0454166). The authors also thank Yvonne Hora at the Monash X-ray Platform for assistance and Peng Zhou for guidance with SEM operations. Open access publishing facilitated by Monash University, as part of the Wiley - Monash University agreement via the Council of Australian University Librarians. Open Access publishing facilitated by Monash University, as part of the Wiley - Monash University agreement via the Council of Australian University Librarians.

Conflict of Interest

The authors declare no conflict of interest.

Data Availability Statement

The data that support the findings of this study are available from the corresponding author upon reasonable request.

Keywords: Carbon Gas Diffusion Layer · Electrochemical CO_2 Reduction · Hydrophobicity Graded · Hydrophobicity and Pore Size Control · Polytetrafluoroethylene

[1] a) F. Li, S. F. Zhao, L. Chen, A. Khan, D. R. MacFarlane, J. Zhang, *Energy Environ. Sci.* **2016**, *9*, 216–223; b) C. Xiao, J. Zhang, *ACS Nano* **2021**, *15*, 7975–8000; c) J. Gu, C. S. Hsu, L. Bai, H. M. Chen, X. Hu, *Science* **2019**, *364*, 1091–1094; d) K. U. Hansen, F. Jiao, *Joule* **2021**, *5*, 754–757; e) M. Li, H. Wang, W. Luo, P. C. Sherrell, J. Chen, J. Yang, *Adv. Mater.* **2020**, *32*, 2001848.

[2] a) M. Jouny, W. Luc, F. Jiao, *Ind. Eng. Chem. Res.* **2018**, *57*, 2165–2177; b) H. Shin, K. U. Hansen, F. Jiao, *Nat. Sustainability* **2021**, *4*, 911–919.

[3] a) C. S. Wong, P. Y. Tishchenko, W. K. Johnson, *J. Chem. Eng. Data* **2005**, *50*, 817–821; b) D. Wakerley, S. Lamaison, F. Ozanam, N. Menguy, D. Mercier, P. Marcus, M. Fontecave, V. Mougel, *Nat. Mater.* **2019**, *18*, 1222–1227; c) C. T. Dinh, T. Burdyny, G. Kibria, A. Seifitokaldani, C. M. Gabardo, F. Pelayo García De Arquer, A. Kiani, J. P. Edwards, P. De Luna, O. S. Bushuyev, C. Zou, R. Quintero-Bermudez, Y. Pang, D. Sinton, E. H. Sargent, *Science* **2018**, *360*, 783–787; d) Y. Y. Birdja, E. Pérez-Gallent, M. C. Figueiredo, A. J. Göttle, F. Calle-Vallejo, M. T. M. Koper, *Nat. Energy* **2019**, *4*, 732–745.

[4] a) D. M. Weekes, D. A. Salvatore, A. Reyes, A. Huang, C. P. Berlinguette, *Acc. Chem. Res.* **2018**, *51*, 910–918; b) D. Higgins, C. Hahn, C. Xiang, T. F. Jaramillo, A. Z. Weber, *ACS Energy Lett.* **2019**, *4*, 317–324; c) L. Fan, C. Xia, F. Yang, J. Wang, H. Wang, Y. Lu, *Sci. Adv.* **2020**, *6*, eaay3111; d) C. Kim, J. C. Bui, X. Luo, J. K. Cooper, A. Kusoglu, A. Z. Weber, A. T. Bell, *Nat. Energy* **2021**, *6*, 1026–1034.

[5] a) E. L. Clark, J. Resasco, A. Landers, J. Lin, L. T. Chung, A. Walton, C. Hahn, T. F. Jaramillo, A. T. Bell, *ACS Catal.* **2018**, *8*, 6560–6570; b) B. A. Zhang, T. Ozel, J. S. Elias, C. Costentin, D. G. Nocera, *ACS Cent. Sci.* **2019**, *5*, 1097–1105; c) T. Burdyny, P. J. Graham, Y. Pang, C. T. Dinh, M. Liu, E. H. Sargent, D. Sinton, *ACS Sustainable Chem. Eng.* **2017**, *5*, 4031–4040; d) T. Burdyny, W. A. Smith, *Energy Environ. Sci.* **2019**, *12*, 1442–1453; e) L. C. Weng, A. T. Bell, A. Z. Weber, *Phys. Chem. Chem. Phys.* **2018**, *20*, 16973–16984; f) F. P. García de Arquer, C. T. Dinh, A. Ozden, J. Wicks, C. McCallum, A. R. Kirmani, D. H. Nam, C. Gabardo, A. Seifitokaldani, X. Wang, Y. C. Li, F. Li, J. Edwards, L. J. Richter, S. J. Thorpe, D. Sinton, E. H. Sargent, *Science* **2020**, *367*, 661–666.

[6] Z. Xing, L. Hu, D. S. Ripatti, X. Hu, X. Feng, *Nat. Commun.* **2021**, *12*, 136.

[7] a) F. Li, A. Thevenon, A. Rosas-Hernández, Z. Wang, Y. Li, C. M. Gabardo, A. Ozden, C. T. Dinh, J. Li, Y. Wang, J. P. Edwards, Y. Xu, C. McCallum, L. Tao, Z. Q. Liang, M. Luo, X. Wang, H. Li, C. P. O'Brien, C. S. Tan, D. H. Nam, R. Quintero-Bermudez, T. T. Zhuang, Y. C. Li, Z. Han, R. D. Britt, D. Sinton, T. Agapie, J. C. Peters, E. H. Sargent, *Nature* **2020**, *577*, 509–513; b) C. M. Gabardo, A. Seifitokaldani, J. P. Edwards, C. T. Dinh, T. Burdyny, M. G. Kibria, C. P. O'Brien, E. H. Sargent, D. Sinton, *Energy Environ. Sci.* **2018**, *11*, 2531–2539; c) B. Kim, F. Hillman, M. Ariyoshi, S. Fujikawa, P. J. A. Kenis, *J. Power Sources* **2016**, *312*, 192–198.

[8] a) K. Ehelebe, J. Knöppel, M. Bierling, B. Mayerhöfer, T. Böhm, N. Kulyk, S. Thiele, K. J. J. Mayrhofer, S. Cherevko, *Angew. Chem. Int. Ed.* **2021**, *60*, 8882–8888; *Angew. Chem.* **2021**, *133*, 8964–8970; b) J. Schröder, V. A. Mints, A. Bornet, E. Berner, M. Fathi Tovini, J. Quinson, G. K. H. Wiberg, F. Bizzotto, H. A. El-Sayed, M. Arenz, *JACS Au* **2021**, *1*, 247–251.

[9] a) M. E. Leonard, L. E. Clarke, A. Forner-Cuenca, S. M. Brown, F. R. Brushett, *ChemSusChem* **2020**, *13*, 400–411; b) M. Jouny, W. Luc, F. Jiao, *Nat. Catal.* **2018**, *1*, 748–755.

[10] a) S. Verma, Y. Hamasaki, C. Kim, W. Huang, S. Lu, H. R. M. Jhong, A. A. Gewirth, T. Fujigaya, N. Nakashima, P. J. A. Kenis, *ACS Energy Lett.* **2018**, *3*, 193–198; b) K. Yang, R. Kas, W. A. Smith, T. Burdyny, *ACS Energy Lett.* **2021**, *6*, 33–40; c) E. W. Lees, B. A. W. Mowbray, F. G. L. Parlane, C. P. Berlinguette, *Nat. Rev. Mater.* **2022**, *7*, 55–64.

[11] B. De Mot, J. Hereijgers, M. Duarte, T. Breugelmans, *Chem. Eng. J.* **2019**, *378*, 122224.

[12] R. Shi, J. Guo, X. Zhang, G. I. N. Waterhouse, Z. Han, Y. Zhao, L. Shang, C. Zhou, L. Jiang, T. Zhang, *Nat. Commun.* **2020**, *11*, 3028.

[13] S. Park, J. W. Lee, B. N. Popov, *Int. J. Hydrogen Energy* **2012**, *37*, 5850–5865.

[14] A. Ozden, F. Li, F. P. GarcÍa De Arquer, A. Rosas-Hernández, A. Thevenon, Y. Wang, S. F. Hung, X. Wang, B. Chen, J. Li, J. Wicks, M. Luo, Z. Wang, T. Agapie, J. C. Peters, E. H. Sargent, D. Sinton, *ACS Energy Lett.* **2020**, *5*, 2811–2818.

[15] M. Zhong, K. Tran, Y. Min, C. Wang, Z. Wang, C.-T. Dinh, P. De Luna, Z. Yu, A. S. Rasouli, P. Brodersen, S. Sun, O. Voznyy, C.-S. Tan, M. Askerka, F. Che, M. Liu, A. Seifitokaldani, Y. Pang, S.-C. Lo, A. Ip, Z. Ulissi, E. H. Sargent, *Nature* **2020**, *581*, 178–183.

[16] Y. Liang, H. Zhang, J. Zhang, X. Cheng, Y. Zhu, L. Luo, S. Lu, J. Wei, H. Wang, *Electrochim. Acta* **2020**, *332*, 135397.

[17] a) T. S. Galhardo, A. H. Braga, B. H. Arpini, J. Szanyi, R. V. Gonçalves, B. F. Zornio, C. R. Miranda, L. M. Rossi, *J. Am. Chem. Soc.* **2021**, *143*, 4268–4280; b) W. Ju, A. Bagger, G. P. Hao, A. S. Varela, I. Sinev, V. Bon, B. Roldan Cuenya, S. Kaskel, J. Rossmeisl, P. Strasser, *Nat. Commun.* **2017**, *8*, 944.

[18] G. Mattogno, C. Ferragina, M. A. Massucci, P. Patrono, A. La Ginestra, *J. Electron Spectrosc. Relat. Phenom.* **1988**, *46*, 285–295.
[19] a) M. C. Biesinger, B. P. Payne, L. W. M. Lau, A. Gerson, R. S. C. Smart, *Surf. Interface Anal.* **2009**, *41*, 324–332; b) M. C. Biesinger, L. W. M. Lau, A. R. Gerson, R. S. C. Smart, *Phys. Chem. Chem. Phys.* **2012**, *14*, 2434–2442.
[20] J. V. Rojas, M. Toro-Gonzalez, M. C. Molina-Higgins, C. E. Castano, *Mater. Sci. Eng. B* **2016**, *205*, 28–35.
[21] M. Cologna, in *Compr. Nucl. Mater., Vol. 5*, Elsevier, Amsterdam, **2020**, pp. 811–839.
[22] J. Sim, M. Kang, K. Min, *Int. J. Hydrogen Energy* **2021**, *46*, 18615–18629.
[23] W. Luc, J. Rosen, F. Jiao, *Catal. Today* **2017**, *288*, 79–84.

Manuscript received: June 10, 2022
Accepted manuscript online: August 4, 2022
Version of record online: August 23, 2022